RESEARCH ARTICLE

CARBON ENERGY WILEY

Sulfur-doped hard carbon hybrid anodes with dual lithium-ion/metal storage bifunctionality for high-energy-density lithium-ion batteries

Sungmin Cho[1] | Jong Chan Hyun[2] | Son Ha[2] | Yeonhua Choi[2] |
Honggyu Seong[3] ⓘ | Jaewon Choi[3] | Hyoung-Joon Jin[1,4] | Young Soo Yun[2,5] ⓘ

[1]Program in Environmental and Polymer Engineering, Inha University, Incheon, South Korea

[2]KU-KIST Graduate School of Converging Science and Technology, Korea University, Seoul, South Korea

[3]Departmant of Chemistry and Research Institute of Natural Science, Gyeongsang National University, Jinju, South Korea

[4]Department of Polymer Science and Engineering, Inha University, Incheon, South Korea

[5]Division of Energy Engineering, Kangwon National University, Gangwon-do, South Korea

Correspondence
Young Soo Yun, KU-KIST Graduate School of Converging Science and Technology, Korea University, 145 Anam-ro, Seongbuk-gu, Seoul 02841, South Korea.
Email: c-ysyun@korea.ac.kr

Hyoung-Joon Jin, Department of Polymer Science and Engineering, Inha University, 100 Inha-ro, Michuhol-gu, Incheon 22212, South Korea.
Email: hjjin@inha.ac.kr

Funding information
Kangwon National University, Grant/Award Number: 2018 Research Grant (PoINT); National Research Foundation of Korea, Grant/Award Numbers: 2019R1A2C1084836, 2021R1A4A2001403

Abstract

Bifunctional hybrid anodes (BHAs), which are both a high-performance active host material for lithium-ion storage as well as a guiding agent for homogeneous lithium metal nucleation and growth, exhibit significant potential as anodes for next-generation high-energy-density lithium-ion batteries (LIBs). In this study, sulfur-doped hard carbon nanosphere assemblies (S-HCNAs) were prepared through a hydrothermal treatment of a liquid organic precursor, followed by high-temperature thermal annealing with elemental sulfur for application as BHAs for LIBs. In a carbonate-based electrolyte containing fluoroethylene carbonate additive, the S-HCNAs showed high lithium-ion storage capacities in sloping as well as plateau voltage sections, good rate capabilities, and stable cyclabilities. In addition, high average Coulombic efficiencies (CEs) of ~96.9% were achieved for dual lithium-ion and lithium metal storage cycles. In the LIB full-cell tests with typical NCM811 cathodes, the S-HCNA-based BHAs containing ~400 mA h g^{-1} of excess lithium led to high energy and power densities of ~500 W h kg^{-1} and ~1695 W kg^{-1}, respectively, and a stable cycling performance with ~100% CEs was achieved.

KEYWORDS
hard carbon, hybrid anode, lithium-ion batteries, lithium metal anode, lithium metal batteries, sulfur-doped carbon

1 | INTRODUCTION

Rechargeable lithium-ion batteries (LIBs) based on a pair of active host materials exhibit high round-trip efficiency, stable cyclability, and competitive energy density, and these unique properties have resulted in their widespread use in portable electronic devices and electric vehicles.[1-3] However, the designated charge storage sites of the host materials significantly restrict lithium-ion redox capacities, which hinders the development of advanced LIBs to meet the changing demands in the new industrial epoch.[4-6] In addition, sluggish lithium-ion migration via solid-state diffusion in the long-range-ordered host structure results in large overpotentials and low rate capabilities.[7-10] These apparent disadvantages necessitate the development of high-performance anode materials, and a variety of suitable anode materials, such as metal oxide/sulfide, silicon, tin, and carbon-based materials, have been considered as potential candidates.[11-19] However, the application of these anode materials is limited by several complicated issues, such as large voltage hysteresis, large volume changes, poor Coulombic efficiencies (CEs), and insufficient cycling stabilities. Therefore, these newly developed materials have considerable limitations to overcome for surpassing the overall electrochemical performance of typical graphite-based anodes in LIBs.[20-23]

Owing to a lack of feasible alternative anode materials and the urgent need for high-energy-density LIBs, considerable efforts are being devoted to the study of lithium metal anodes (LMAs) because of their high theoretical capacity of 3860 mA h g^{-1} and low redox potential of −3.04 V (vs. SHE). High-capacity LMAs can deliver a significantly more number of charges than those of typical graphite through a small amount of mass loading and can recover the lithium loss that occurs during the charge/discharge process. This enables a sharp increase in specific energy density and 100% CEs during cycling.[24-28] However, critical issues persist in the application of LMAs, such as unexpected dendritic lithium metal growth, consecutive electrolyte consumption, large volume changes, low CEs, a substantial increase of overpotentials, and poor cell stabilities.[29-32] These issues can be mitigated by introducing three-dimensional-structured lithiophilic electrodes (3D-LEs); their high lithiophilicity and large surface areas can facilitate homogeneous lithium metal nucleation and growth in extensive surfaces, and the inner spaces of the 3D structure can accommodate lithium metals with insignificant changes in volume.[33-35] Furthermore, if the 3D-LEs are used as active host materials, considerable merits of both 3D-LEs and active host materials can be utilized as a bifunctional hybrid anode (BHA). Additionally, the introduction of BHAs can reduce excess lithium metal loading owing to the presence of highly reversible active host materials, thereby increasing battery safety.[36,37] The potential advantage of using BHAs was demonstrated by Martin et al., who revealed that the BHA with a bulk graphite reduces the stack mass loading density by approximately 85% in comparison to conventional LIBs, leading to an enhancement in energy density by ~19%.[38] The synergistic effect can be improved using active host materials, which are more lithiophilic and have higher active surface areas. However, many previous reports have focused only on the functionality of the 3D-LEs, and negligible attention has been paid to BHAs despite their high potential for application in excess lithium-aided LIBs (EL-LIBs).[39-41]

This study presents high-performance BHAs based on sulfur-doped hard carbon nanosphere assemblies (S-HCNAs). The effects of electrolyte additives, such as vinylene carbonate (VC) and fluoroethylene carbonate (FEC), on the BHAs were studied through experimental comparison to improve dual lithium-ion and metal storage performance in carbonate-based electrolyte systems. The S-HCNA-based BHAs demonstrated a high electrochemical performance in both lithium-ion and metal storage and exhibited significant potential in the full-cell tests. This study is the first to prove the practicality of using EL-LIBs employing BHAs as next-generation high-energy-density LIBs.

2 | EXPERIMENTAL SECTION

2.1 | Preparation of S-HCNAs

First, 0.3 M sucrose solution was prepared by dissolving 14.36 g of sucrose in 140 mL of distilled (DI) water for 1 h. The solution was then heated up to 180°C and held for 4 h in a PTFE-lined stainless-steel autoclave. After cooling the autoclave naturally, the products obtained were centrifuged at 9500 rpm for 30 min and washed with DI water and ethanol. The as-obtained products were then physically mixed with 500 wt.% elemental sulfur in a mortar, and the resulting mixture was annealed at 1200°C for 2 h in a tube furnace. A heating rate of 5°C min^{-1} was applied in the annealing process, under a 50 mL min^{-1} Ar flow. The final products, S-HCNAs, were obtained after naturally cooling the tube furnace. An identical fabrication process without elemental sulfur was applied to obtain the HCNAs.

2.2 | Characterization

Morphologies of the S-HCNAs and HCNAs were observed through high-resolution transmission electron microscopy

(HR-TEM) (JEM2100F; JEOL) and field emission scanning electron microscopy (FE-SEM, S-4300; Hitachi). Local carbon microstructures of the S-HCNAs and HCNAs were characterized using X-ray diffraction (XRD) (Rigaku DMAX 2500) with a Cu-Kα radiation source ($\lambda = 0.154$ nm, 40 kV, and 100 mA) in the 2θ range of 5°–60°. Surface chemical properties were analyzed using X-ray photoelectron spectroscopy (XPS) (PHI5700 ESCA) with monochromatic Al-Kα radiation. Raman spectroscopy (LabRAM HR Evolution; Horiba) was used to characterize the in-plane carbon microstructure and graphenic domain sizes of the S-HCNAs and HCNAs using a laser (wavelength: 514.5 nm), 1200 groove mm^{-1} grating, and ×2000 objective lens. The porous structures of the S-HCNAs and HCNAs were analyzed via nitrogen adsorption and desorption isotherms obtained using porosimetry and surface area analyzers (ASAP 2460; Micromeritics) at −196°C.

2.3 | Electrochemical characterization

The electrochemical performance of S-HCNAs was characterized using a Wonatech automatic battery cycler and CR2032-coin cells. Coin cells for all electrochemical tests were assembled in a glove box filled with argon gas. The S-HCNA anodes and commercial NCM811 cathodes were prepared via a slurry method as follows: (1) The active material (S-HCNA or NCM811), polyvinylidene fluoride binder, and conducting carbon were mixed in a weight ratio of 8:1:1 in N-methyl-2-pyrrolidone solvent. (2) The mixture was cast on Cu or Al foil. (3) The coated slurry was dried at 80°C for 30 min in a vacuum oven. The working electrodes were prepared by puncturing the S-HCNA anode or NCM811 cathode to obtain 1/2-inch pieces. A metallic Li foil was used as both the reference and counter electrodes, and a glass microfiber filter (GF/F, Whatman) was used as the separator for the half-cell tests. The electrolyte was prepared by dissolving 1.0 M LiPF$_6$ (Sigma-Aldrich) in a DMC and EC solution (1:1ν/ν). For the half-cell tests, the galvanostatic discharge/charge process was conducted at 20 mA g^{-1} in an operating voltage window of 0.01 to 2.70 V versus Li$^+$/Li, and the galvanostatic lithium metal deposition/dissolution cycles were measured at different current densities from 80 to 6400 mA g^{-1}, with a cut-off capacity of 800 m A h g^{-1}. Electrochemical impedance spectroscopy (EIS) was performed at room temperature over a 1 mHz–1 MHz frequency range. For the full-cell tests, precycled S-HCNA anodes and NCM811 cathodes were extracted from their respective half-cells and reassembled as full cells. The electrochemical performance of the full cells was characterized at 20 mA g^{-1} in a voltage window of 2.7–4.4 V.

3 | RESULTS AND DISCUSSION

The S-HCNAs exhibit a 3D-macroporous structure composed of interconnected uniform nanospheres approximately 500 nm in diameter (Figure 1A,B). The HR-TEM image reveals a highly complex microstructure consisting of poorly developed graphitic lattices, which are randomly oriented on the overall surfaces (Figure 1C). The blur graphite (002) and (100) ring patterns of the selected area diffraction suggest the presence of a not well-ordered graphitic structure (inset of Figure 1C). The d-spacing of the graphitic lattices, calculated from the HR-TEM image, exhibits a broad range of 3.4–4.2 Å, and the structure is dominated by expanded lattices with spacings of approximately 3.7–4.0 Å (Figure 1D). The microstructure of the S-HCNAs was analyzed in significant detail via XRD and Raman spectroscopy (Figure 1E,F). The XRD pattern exhibits a broad graphite (002) peak at 23.5°, corresponding to a d-spacing of 3.8 Å, which is in strong agreement with the HR-TEM analysis results (Figure 1E). In addition, the Raman spectrum exhibits a relatively large D (~1331 cm^{-1}) to G band (~1573 cm^{-1}) intensity ratio (Figure 1F). Because the D band is induced by the asymmetric vibration of the six-membered carbon rings, the large D band intensity indicates the presence of a large number of defects, which deform the ordered polyhexagonal planes. Hence, the XRD pattern and Raman spectrum collectively reveal that topological defects deform the planar graphenic carbon domains of the S-HCNAs, resulting in expanded and not well-ordered graphitic structures. Similar morphology and microstructure are observed in the HCNA fabricated without any sulfur dopants, indicating that the sulfur molecules affected neither the 3D-macroporous morphology nor the microstructures comprising spherical primary particles during the fabrication process (Figure S1).

Surface chemical structures of the S-HCNAs were characterized through XPS analysis (Figure 1G,H). The C 1s spectrum reveals two distinctive carbon bonds at 284.4 and 285.2 eV corresponding to C=C and C-C/C-S, respectively, and minor C–O and C=O bonds are also confirmed at 284.4 and 285.2 eV respectively (Figure 1G). In the S 2p spectrum, C–S and C=S bonds are mainly observed with a minor C–SO$_x$ bond (Figure 1H). The S/C atomic ratio is ~0.05, and the specific sulfur content in the S-HCNAs is confirmed as 4.8 wt.% via elemental analysis. The sulfur content of the S-HCNAs is also more than twice that of
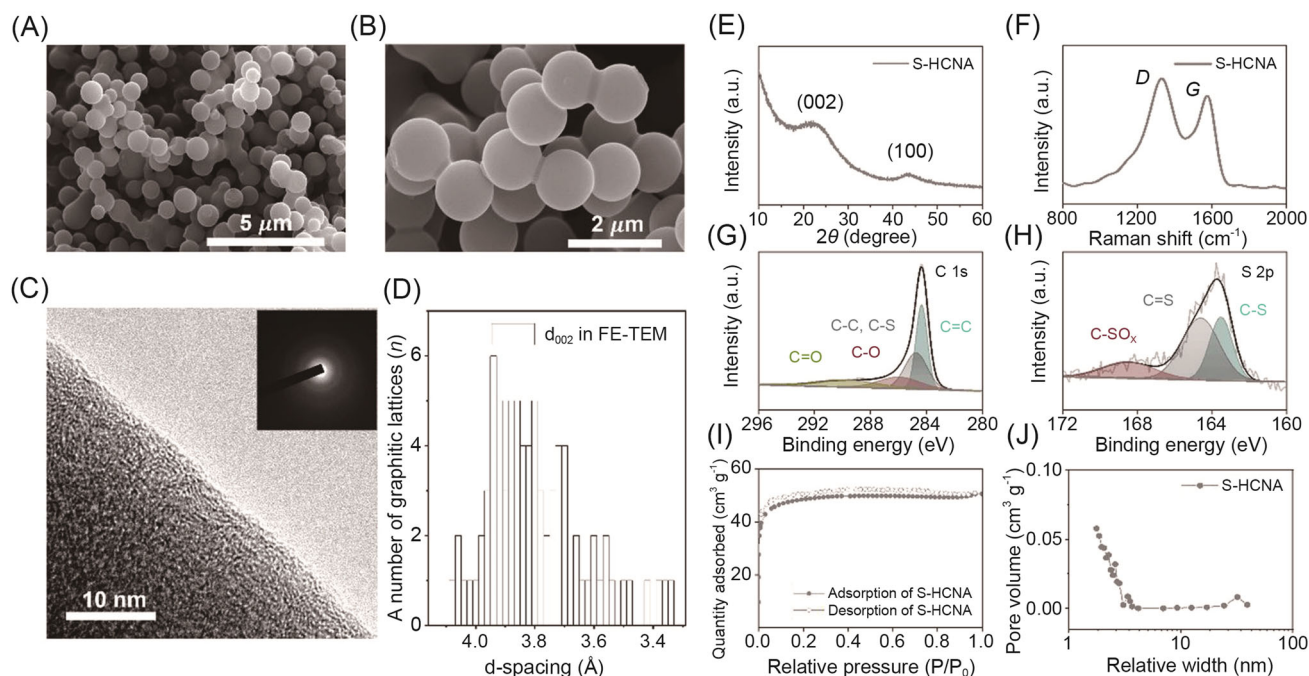
FIGURE 1 Material properties of S-HCNAs. (A,B) FE-SEM images at different magnifications. (C) High-resolution FE-TEM image and the inset presenting the selective area diffraction pattern; (D) d-spacing variation. (E) XRD pattern, (F) Raman spectrum, XPS (G) C 1s and (H) S 2p profiles, (I) nitrogen adsorption–desorption isotherms, and (J) pore size distribution. FE-SEM, field emission scanning electron microscopy; FE-TEM, field emission transmission electron microscopy; S-HCNAs, sulfur-doped hard carbon nanosphere assemblies; XPS, X-ray photoelectron spectroscopy; XRD, X-ray diffraction.

previously reported sulfur-doped graphene (S/C ratio: 0.02).[42]

Porous properties of the S-HCNAs were analyzed via nitrogen adsorption and desorption isotherm tests (Figure 1I). The isotherm curves show a sharp increase in the quantity of adsorbed nitrogen over the initial relative pressure region, indicating that the S-HCNAs have a large open surface area for monolayer nitrogen adsorption. The S-HCNAs also have a specific surface area of $\sim150 \, \text{m}^2 \, \text{g}^{-1}$, which is a much higher value than that of typical graphite-based materials ($<2 \, \text{m}^2 \, \text{g}^{-1}$). Pore size distribution data obtained using the Barrett–Joyner–Halenda method shows that the S-HCNAs have multitudinous micropores of <2 nm as well as macropores, as observed in Figure 1A,B.

An in-depth analysis of the material properties of S-HCNAs reveals their significant application potential as BHAs for EL-LIBs. The S-HCNAs have a disordered graphitic structure consisting of a large number of defects, which can serve as redox hosts for lithium-ion storage. The high specific surface area of S-HCNAs with enriched sulfur dopants can facilitate their application as a lithiophilic catalytic substrate to enable homogeneous lithium metal nucleation and growth. Moreover, nanoscale pores developed on the lithiophilic surfaces can facilitate lithium metal nucleation, and the macropores can accommodate the deposited lithium metal with the

negligible volume change, thereby providing optimal bimodal pore structures for lithium metal storage. The twofold lithium-ion and metal storage performance of the S-HCNAs was examined through galvanostatic discharge/charge tests, and the effects of electrolyte additives and sulfur functional groups on their electrochemical performance were confirmed through comparative experiments.

Electrochemical lithium-ion storage performance of S-HCNAs was investigated in a lithium half-cell using a carbonate-based electrolyte system composed of 1 M $LiPF_6$ and ethylene carbonate (EC)/dimethyl carbonate (DMC) mixture solution (1:1 v/v). The tests were performed both without an additive and with 5 wt.% VC and 5 wt.% FEC additives (Figure 2). In the operating voltage window between 0.01 and 2.70 V versus Li^+/Li, all the lithiation profiles obtained using the different electrolyte systems exhibit two distinctive charge storage sections—a sloping capacity region (C_s), followed by a plateau capacity region (C_p) (Figure 2A). The C_s is attributed to lithium-ion chemisorption in the numerous defect sites and its insertion into the disordered graphitic lattice sites. With increasing lithiation capacity, the chemical potential gap ($\Delta\mu$) between lithiated S-HCNA and the lithium metal continuously decreases, leading to a linear voltage drop (Figure S2). In contrast, the
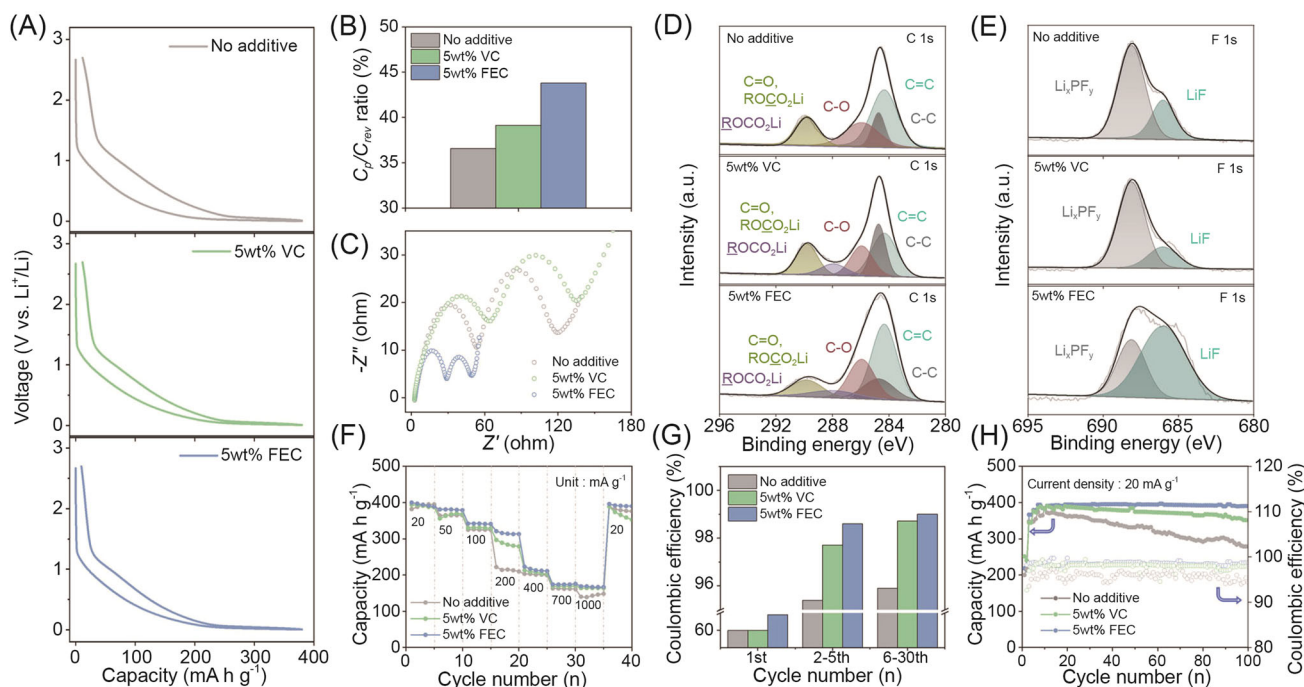
FIGURE 2 Electrochemical performances of S-HCNAs for lithium-ion storage over a voltage window of 0.01–2.70 V versus Li+/Li in different carbonate-based electrolyte systems (1 M LiPF$_6$ in EC/DMC (1:1 v/v) with no, 5 wt.% VC, and 5 wt.% FEC additives). (A) Galvanostatic discharge/charge profiles at 20 mA g^{-1}, (B) bar graphs for the C_p/C_{rev} ratios, (C) EIS profiles at frequencies between 1 mHz and 1 MHz characterized after full lithiation, ex situ XPS (D) C 1 s and (E) F 1s profiles measured after the initial cycle, (F) rate capabilities at current densities from 20 to 1000 mA g^{-1}, (G) average CE bar graphs at different cycle numbers, and (H) cycling performances including CE values. CE, Coulombic efficiency; DMC, dimethyl carbonate; EC, ethylene carbonate; EIS, electrochemical impedance spectroscopy; FEC, fluoroethylene carbonate; S-HCNAs, sulfur-doped hard carbon nanosphere assemblies; VC, vinylene carbonate; XPS, X-ray photoelectron spectroscopy.

presence of the following C_p suggests the formation of a new lithiation phase at ~0 V. This phase may originate from pore filling that occurs through lithium nanocluster formation on the internal closed pores of the S-HCNAs (Figure S2). The overall reversible capacities (C_{rev}) of the S-HCNAs were generally similar with values of ~368, ~369, and ~371 mA h g^{-1} in the electrolyte systems without additives, with VC and with FEC additives, respectively, whereas the C_p/C_{rev} ratio varied according to additives (Figure 2A,B). In the FEC-added electrolyte, the C_p/C_{rev} ratio was approximately 43.8%, which is 4.7% and 7.2% higher than those of additive-free and VC-added electrolytes, respectively (Figure 2B). In addition, the voltage hysteresis between the discharge/charge profiles was much lower in the FEC-added electrolyte, thereby demonstrating its higher energy efficiency (Figure 2A). EIS profiles revealed that the different plateau capacities and voltage hysteresis values were due to the differences in surface film resistance (R_f) and charge transfer resistance (R_{ct}) (Figure 2C). The R_f/R_{ct} values of the S-HCNAs were approximately 53/67, 64/70, and 28/21 Ω in the additive-free, VC-added, and FEC-added electrolytes, respectively. The much lower R_f value in the FEC-added

electrolyte implies that more conductive and/or thinner solid-electrolyte interface (SEI) layers were formed with the FEC additive on the surface of the S-HCNAs. Moreover, the significantly lower R_{ct} value indicates the highly advantageous effects of FEC additives on the charge transfer kinetics of S-HCNAs. Ex situ XPS analysis data show clear differences in the SEI composition of the S-HCNAs in the different electrolyte systems following the initial cycle (Figure 2D,E). The ex situ XPS C 1 s spectra of the S-HCNAs cycled in the different electrolytes revealed that the highest sp^3-structured carbon bonding intensity was observed for the S-HCNAs cycled in the VC-added electrolyte (Figure 2D). In addition, the ex situ F 1s spectra show that inorganic LiF content was reduced while using the VC additive, while the use of the FEC additive significantly increased the LiF content (Figure 2E). These results suggest that the inorganic SEI component is a key factor allowing the enhanced lithium-ion migration and charge-transfer kinetics, as observed in Figure 2C. The FEC-induced SEI layer also led to the lower R_f and R_{ct} values, which retarded the low voltage cut-off and led to the consequential increase in the C_p values (Figure 2B). The FEC-induced SEI layer also shows enhanced rate

capabilities and reversibility in the current densities from 20 to 1000 mA g^{-1} (Figure 2F). More importantly, CE values were significantly improved while using the FEC additive (Figure 2G). The CE value of the FEC-added electrolyte was ~4.5% higher than that of the additive-free and VC-added electrolytes in the first cycle, and the higher CE value was maintained during the successive cycles. In the 2–5th and 6–30th cycles, average CE values of ~98.6% and 99% were achieved, respectively. These are 3.2/3.1% and 0.9/0.3% higher than those of the additive-free and VC-added electrolytes, respectively. The higher CE values led to more stable cycling behaviors, wherein the initial C_{rev} values were well-maintained during cycling for over 100 cycles (Figure 2H). Additionally, the effects of sulfur functional groups and heating temperatures on the lithium-ion storage performances were compared in a similar lithium half-cell system (Figures S3–S5). In all the galvanostatic discharge/charge profiles of the HCNAs with no sulfur dopants, larger voltage hysteresis values were confirmed at the sloping voltage section regardless of electrolyte additives (Figure S3). In addition, CE values of the HCNAs are overall lower than those of the S-HCNAs (Figure S4 and Table S1), supporting that sulfur dopants can improve the reversibility of the lithium-ion redox reactions in hard carbon structures. Moreover, heating temperatures strongly affect the lithium-ion storage capacities. The lower or higher heating temperatures than the target temperature, 1200°C, for the fabrication of S-HCNAs led to the reduction of reversible capacities from ~14 to ~52%, wherein the S-HCNAs prepared at 1200°C were used for the target hybrid anode (Figure S5). The superiority of S-HCNAs for lithium-ion storage perform-ances can be confirmed in Table S2, where the CE values, reversible capacity, and capacity retention of S-HCNAs are higher than those of previously reported hard carbon materials.[43–47]

To investigate the hybrid lithium-ion and metal storage performance of the S-HCNAs in the different electrolyte systems, galvanostatic lithiation–delithiation tests were conducted with a cut-off capacity of 800 mA h g^{-1}; this is approximately composed of a half and half ratio for lithium-ion and metal storage capacities, respectively. The catalytic ability for lithium metal nucleation was characterized using the voltage gap between the lowest voltage and proceeding plateau voltage and is denoted as the lithium-metal nucleation overpotential (η_n), as shown in Figure S6. Despite using the same electrodes in the experimental runs, large differences in the η_n values were observed according to the electrolyte systems (Figure 3A–C). In the additive-free electrolyte, the η_n value was ~18 mV, which increased to ~23 mV in the VC-added electrolyte (Figure 3A,B). In contrast, the η_n value in the FEC-

added electrolyte was significantly reduced to ~13 mV (Figure 3C). The sizable variation of η_n values results from the different SEI layers because lithium metal nucleation occurs in the solid–solid interface between the S-HCNA and the SEI layer.[48,49] According to the conventional nucleation theory, lithium metal nucleation is limited by interfacial surface energy (Υ), which can be reduced by the formation of more lithiophilic solid interfaces.[50,51] Therefore, the lower η_n value of the FEC-induced inorganic-rich SEI layer indicates that it has better lithiophilicity, thereby demonstrating that the FEC additive is very effective in enhancing the lithium-ion and metal storage characteristics of the S-HCNAs.

The electrochemical performance of the S-HCNA-based BHAs was further tested at different current densities ranging from 40 to 6400 mA g^{-1} (Figure 3D–F). In the additive-free electrolyte, the galvanostatic lithiation–delithiation profiles show a comparatively lower initial CE value (Figure 3D). In addition, a significant decrease in CE values and large voltage hysteresis is observed with increasing current densities. The initial CE value, voltage hysteresis, and rate capabilities are generally improved in the VC- and FEC-added electrolytes compared to those in the additive-free electrolyte (Figure 3E,F). In particular, voltage hysteresis was reduced considerably, up to ~160 mV in the FEC-added electrolyte. This outcome was observed even at a high current density of 6400 mA g^{-1}, and it was only ~40% of that in the additive-free electrolyte (Figure 3F). Moreover, the higher CE values were well-maintained in the wide current ranges. To elucidate round-trip efficiencies in the different electrolytes, average CE values were measured for the 2nd–30th cycles at different current densities (Figure 3G). In the additive-free electrolyte, the BHAs showed insufficient CE values of 91.7%–76.7% at 0.08–6.4 A g^{-1}, and the values were improved in the VC-added electrolyte to 95.0%–92.2% and further improved to 96.5%–93.9% in the FEC-added electrolyte at the same current density.

For a clear comparison, average CE values of different carbon materials, namely, commercial graphite nano-plates (GNPs) and HCNAs, were analyzed in the different electrolyte systems (Figure 3H). GNPs and HCNAs principally showed lower CE values than the S-HCNAs in the applied current densities, thereby demonstrating the superiority of the disordered graphitic structure over the well-ordered graphite and the positive impact of the sulfur functional groups on the twofold lithium-ion and metal storage performance. Notably, the FEC additive is also highly effective for the GNPs and HCNAs: average CE values were significantly improved by adding VC and FEC additives, from 90.0 to 94.1 and 94.3 for the HCNAs
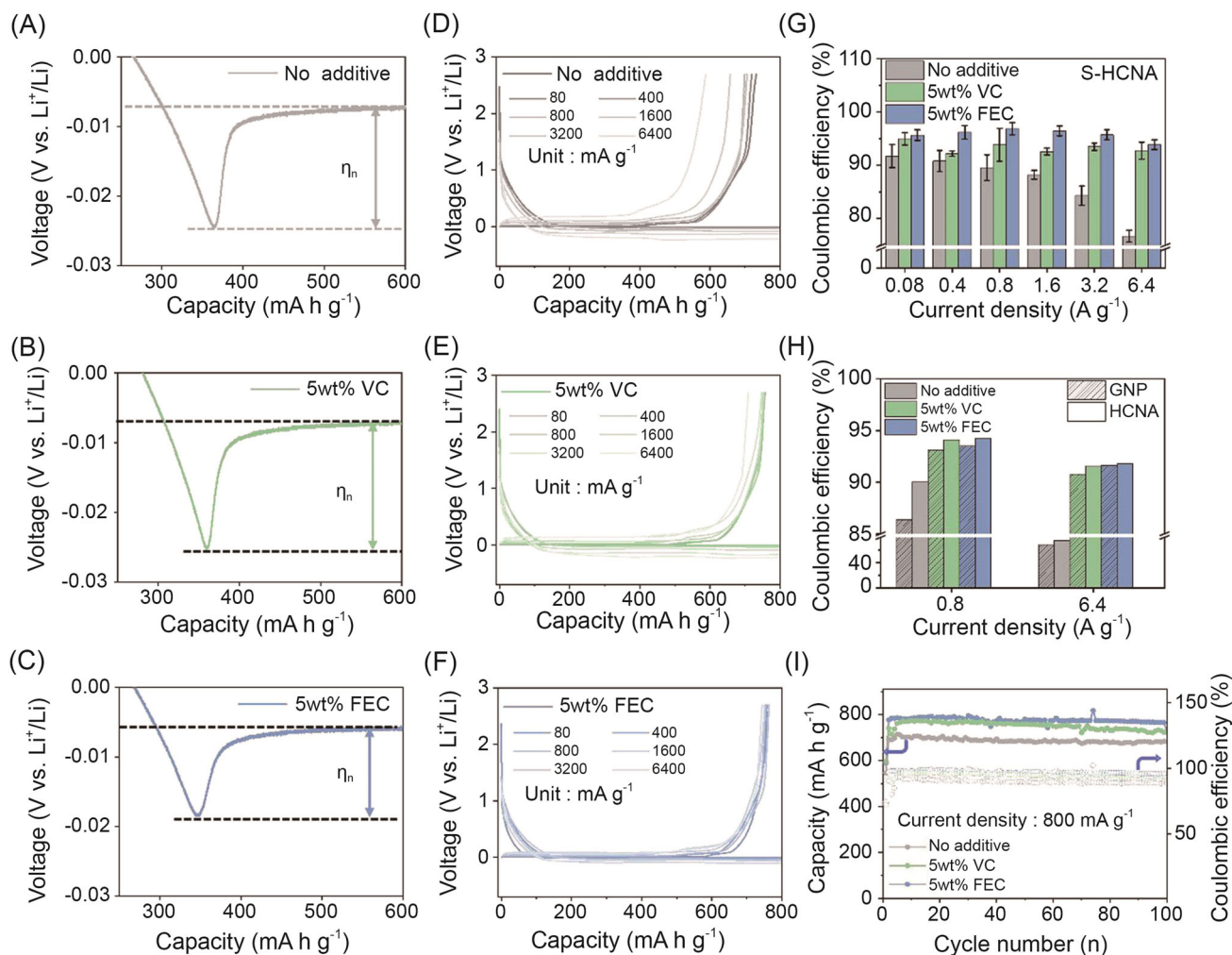
FIGURE 3 Electrochemical performances of the S-HCNA-based BHAs with a cut-off capacity of 800 mA h g^{-1} in different carbonate-based electrolyte systems (1 M LiPF$_6$ in EC/DMC (1:1 v/v) with no, 5 wt.% VC, and 5 wt.% FEC additives). Galvanostatic lithium metal deposition profiles at a current density of 50 mA g^{-1} in the different carbonate-based electrolytes containing (A) no additive, (B) 5 wt.% VC, and (C) 5 wt.% FEC additives. Galvanostatic lithium metal deposition/dissolution profiles at different current densities from 80 to 6400 mA g^{-1} in the different carbonate-based electrolytes containing (D) no additive, (E) 5 wt.% VC, and (F) 5 wt.% FEC additives. Average CE bar graphs of (G) S-HCNA-based BHAs and (H) GNP- and HCNA-based BHAs at different current densities. (I) Cycling performances over 100 cycles at a current density of 800 mA g^{-1}. BHA, bifunctional hybrid anode; CE, Coulombic efficiency; DMC, dimethyl carbonate; EC, ethylene carbonate; FEC, fluoroethylene carbonate; GNP, graphite nanoplates; HCNA, hard carbon nanosphere assemblies; S-HCNA, sulfur-doped hard carbon nanosphere assemblies; VC, vinylene carbonate.

and from 86.4 to 93.1 and 93.5 for the GNPs, respectively, at 0.8 A g^{-1}. Significant increases were also achieved at a higher current density of 6.4 A g^{-1}, where average CE values of 75.1 for the HCNAs increased to 91.6% and 91.8% upon the addition of VC and FEC, respectively; for the GNPs, the addition of VC and FEC led to the increase of average CE values from 68.5% to 90.8% and 91.6%, respectively.

Additionally, the cycling performance of the S-HCNA-based BHAs was characterized by a cut-off lithiation capacity of 800 mA h g^{-1} and a current density of 800 mA g^{-1} in the different electrolyte systems (Figure 3I). Over 100 cycles, average delithiation

capacities of ~693, ~743, and ~767 mA h g^{-1} were achieved in the additive-free, VC-added, and FEC-added electrolyte systems, respectively. This shows that the highest reduction in capacity loss during cycling is achieved in the FEC-added electrolyte system. Ex situ FE-SEM images support the highly stable and efficient cycling behavior of the S-HCNAs in the FEC-added electrolyte, wherein the deposited lithium metal is homogeneously coated on the surface of the spherical S-HCNA particles and can be reversibly removed from the surface (Figure S7A,B). In contrast, nonuniform lithium metal deposition and byproduct formation were observed in the VC-added and additive-free electrolytes
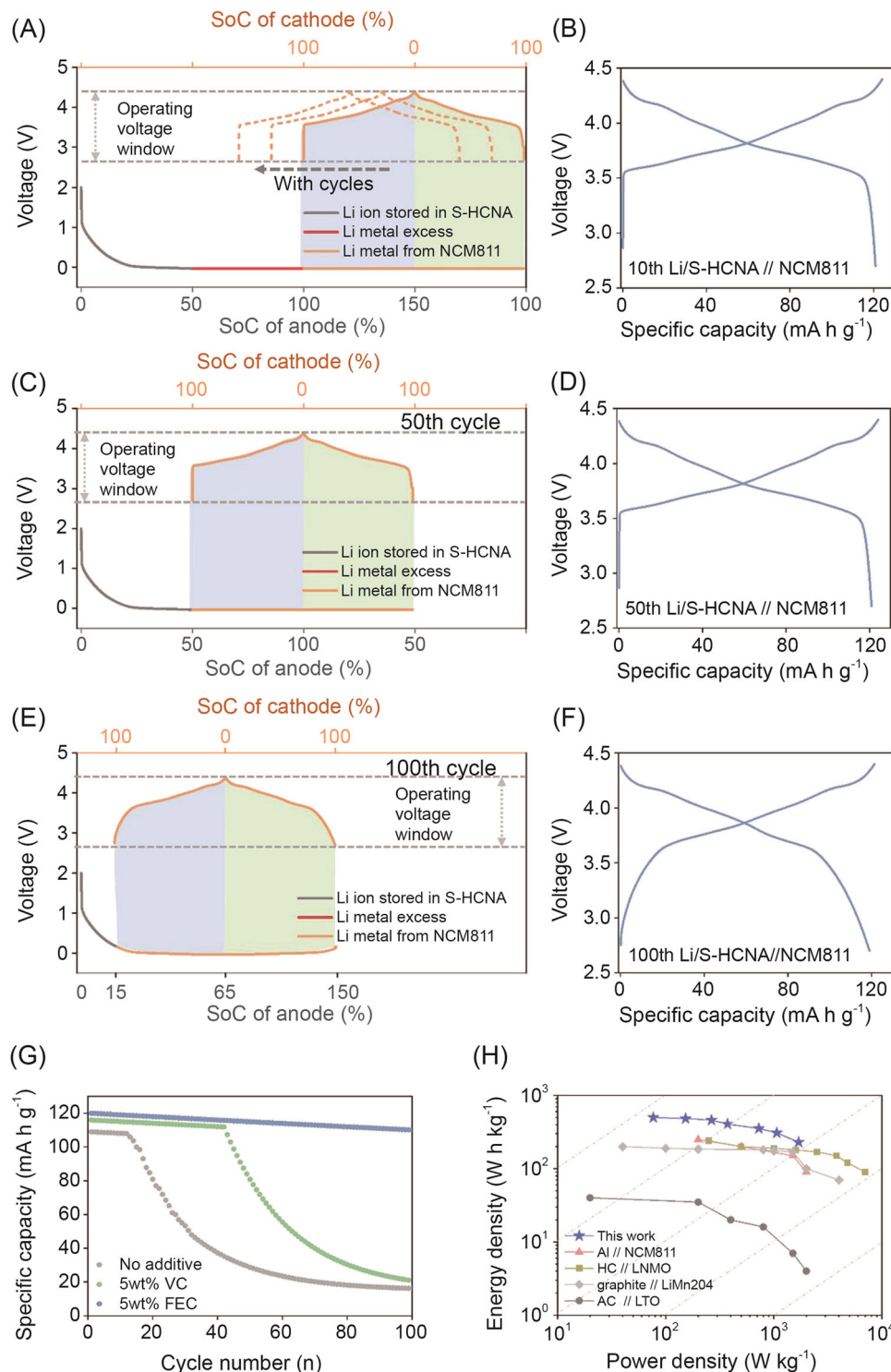
FIGURE 4 Li/S-HCNA-based BHA//NCM811 full cells. Schematics showing galvanostatic profiles of both the anode and cathode at (A) initial, (C) 50th, and (E) 100th cycles. Galvanostatic charge/discharge profiles at (B) initial, (D) 50th, and (F) 100th cycles. (G) Cycling performance in different electrolyte systems and (H) Ragone plots of different energy storage devices, including the Li/S-HCNA-based BHA//NCM811 full cell. BHA, bifunctional hybrid anode; S-HCNA, sulfur-doped hard carbon nanosphere assemblies.

(Figure S7C–F). This observation further highlights the essential nature of the FEC additive in the BHAs. In-situ XRD patterns of the S-HCNAs characterized during the lithiation/delithiation process in the FEC-added electrolyte show no peak change in the overall lithium metal deposition/dissolution process (Figure S8). This result indicates that the homogeneously coated lithium metal is in an amorphous state. In the previously

reported results, it was confirmed that amorphous lithium can guide homogeneous lithium metal growth with no preferred direction, enabling dendrite-free lithium metal deposition/dissolution cycles. Hence, the S-HCNA-based lithium-ion/metal hybrid anode system can be a great strategy for high-energy-density LIBs.[52,53]

To prove the practicality of the S-HCNA-based BHA for application in the EL-LIBs, a full-cell test was conducted using NCM811, which is a typical cathode material. The electrochemical performance of the NCM811 cathode was characterized in a half-cell using the FEC-added electrolyte over a voltage window of 2.7–4.3 V versus Li^+/Li (Figure S9). Galvanostatic charge/discharge curves show C_{rev} and CE values of ~192 mA h g^{-1} and ~99.5%, respectively (Figure S9A). The C_{rev} values gradually decreased with increasing current densities over a continuous 45-cycle span, and the initial C_{rev} was fully recovered when the current density returned to the initial value, thereby indicating appreciable rate capabilities and reversibility (Figure S9B). During 100 cycles, the C_{rev} values continuously decreased, and approximately 82% (~157 mA h g^{-1}) of the initial C_{rev} value was retained in the half-cell cycling test (Figure S9C). An EL-LIB was assembled using BHAs and the NCM811 cathode after galvanostatic pre-cycling in their respective half-cells. For the full-cell assembly, the BHA was lithiated at 800 mA h g^{-1} during the pre-cycling process, and the N/P ratio was designed to be 200%. From the schematic presented in Figure 4A, lithium ions delivered from the NCM811 cathode are deposited/removed on the BHA during the first charge/discharge process. In this process, the state of charge (SoC) of the BHA changes in the 100%–150% range, while the NCM811 is completely charged/discharged. Initial profiles show that the EL-LIBs can deliver C_{rev} values of ~120 mA h g^{-1} at an average voltage of 3.84 V, which corresponds to an energy density of 500 W h kg^{-1} (Figure 4B). In the proceeding charge/discharge cycles, excess lithium metal is gradually consumed to compensate for the lithium loss during the cycling, and the cathode capacities can be fully recovered in approximately 50 cycles despite the irreversible capacities (Figure 4A,C). Therefore, the charge/discharge profiles remained unchanged till the 50th cycle (Figure 4D). As the excess lithium metal is exhausted during the cycling process, the excess lithium-ions stored in S-HCNAs compensate for the lithium loss (Figure 4E), which in turn alters the charge/discharge profiles, leading to a slight decrease of 3.79 V in the average voltage (Figure 4F). Similar cycling experiments were performed in the additive-free and VC-added electrolytes; however, insufficient CE values led to relatively poor cycling performances (Figure 4G, Figures S10, and S11).

Therefore, these results clearly demonstrate the effect of the FEC additive on the performance of full-cell EL-LIBs. In addition, the maximum energy density of the EL-LIBs operated in the FEC-added electrolyte was ~500 W h kg^{-1} at ~77 W kg^{-1}, which gradually decreased with increasing power densities, finally reaching ~230 W h kg^{-1} at ~1695 W kg^{-1} (Figure 4H). The Ragone plot of the EL-LIBs displays their superior relationship between energy and power densities compared with that of previously reported energy storage devices.[54–57] The BHA strategy can be applied in the EL-LIB full-cell system using a different type of carbon materials such as carbon cloth,[58] and much more in-depth studies are needed to build better BHAs for high-energy-density EL-LIBs.

4 | CONCLUSION

S-HCNA-based BHAs were prepared from a liquid organic precursor via hydrothermal synthesis, followed by high-temperature annealing with elemental sulfur. Their lithium-ion/metal storage performance was investigated in different carbonate-based electrolytes, namely, with no, VC, and FEC additives. In the FEC-added carbonate electrolyte system, the S-HCNAs showed high C_{rev} values of ~371 mA h g^{-1}, with a high C_p/C_{rev} ratio of ~43.8 for lithium-ion storage. High average CE values of ~96.9% were also achieved, corresponding to the high cut-off capacity at 800 mA h g^{-1}. The BHAs were used in EL-LIBs with an NCM811 cathode, and the excess lithium supplemented the lithium loss occurring during cycling, ultimately recovering the initial capacities in the 50th cycle. These results demonstrate that highly desirable cycling performances with 100% CE values can be achieved using the BHAs, and the stable cycling numbers can be tuned by controlling the excess lithium loading mass. In addition, EL-LIBs employing the BHAs exhibited better energy and power densities (~500 W h kg^{-1} and ~1695 W kg^{-1}, respectively) than previously reported energy storage devices.

CONFLICTS OF INTEREST
The authors declare no conflicts of interest.

ORCID

Honggyu Seong http://orcid.org/0000-0001-5205-974X
Young Soo Yun https://orcid.org/0000-0002-9643-596X

REFERENCES

1. Duffner F, Kronemeyer N, Tübke J, Leker J, Winter M, Schmuch R. Post-lithium-ion battery cell production and its compatibility with lithium-ion cell production infrastructure. *Nat Energy*. 2021;6(2):123-134.

2. Harper G, Sommerville R, Kendrick E, et al. Recycling lithium-ion batteries from electric vehicles. *Nature*. 2019;575(7781):75-86.

3. Li M, Lu J, Chen Z, Amine K. 30 years of lithium-ion batteries. *Adv Mater*. 2018;30(33):1800561.

4. Lu J, Wu T, Amine K. State-of-the-art characterization techniques for advanced lithium-ion batteries. *Nat Energy*. 2017;2(3):17011.

5. Li L, Zheng Y, Zhang S, Yang J, Shao Z, Guo Z. Recent progress on sodium ion batteries: potential high-performance anodes. *Energy Environ Sci*. 2018;11(9):2310-2340.

6. Sun Y, Zheng G, Seh ZW, et al. Graphite-encapsulated Li-metal hybrid anodes for high-capacity Li batteries. *Chem*. 2016;1(2):287-297.

7. Hu YS, Adelhelm P, Smarsly BM, Hore S, Antonietti M, Maier J. Synthesis of hierarchically porous carbon monoliths with highly ordered microstructure and their application in rechargeable lithium batteries with high-rate capability. *Adv Funct Mater*. 2017;17(12):1873-1878.

8. Li B, Zheng J, Zhang H, et al. Electrode materials, electrolytes, and challenges in nonaqueous lithium-ion capacitors. *Adv Mater*. 2018;30(17):1705670.

9. Roy P, Srivastava SK. Nanostructured anode materials for lithium ion batteries. *J Mater Chem A*. 2015;3(6):2454-2484.

10. Ogihara N, Itou Y, Sasaki T, Takeuchi Y. Impedance spectroscopy characterization of porous electrodes under different electrode thickness using a symmetric cell for high-performance lithium-ion batteries. *J Phys Chem C*. 2015;119(9):4612-4619.

11. Liu B, Zhang JG, Xu W. Advancing lithium metal batteries. *Joule*. 2018;2(5):833-845.

12. Geng P, Zheng S, Tang H, et al. Transition metal sulfides based on graphene for electrochemical energy storage. *Adv Energy Mater*. 2018;8(15):1703259.

13. Jiang H, Liu XC, Wu Y, et al. Metal-organic frameworks for high charge-discharge rates in lithium-sulfur batteries. *Angew Chem Int Ed*. 2018;57(15):3916-3921.

14. Yang Z, Yuan J, Wang S, Chen M. A new hydrophilic binder enabling strongly anchoring polysulfides for high-performance sulfur electrodes in lithium-sulfur battery. *Adv Energy Mater*. 2018;8(12):1702889-1722834.

15. An W, Gao B, Mei S, et al. Scalable synthesis of ant-nest-like bulk porous silicon for high-performance lithium-ion battery anodes. *Nat Commun*. 2019;10:1447.

16. Roland A, Fullenwarth J, Ledeuil JB, Martinez H, Louvain N, Monconduit L. How carbon coating or continuous carbon pitch matrix influence the silicon electrode/electrolyte interfaces and the performance in Li-ion batteries. *Battery Energy*. 2022;1(1):20210009.

17. Zhou X, Wan LJ, Guo YG. Binding SnO_2 nanocrystals in nitrogen-doped graphene sheets as anode materials for lithium-ion batteries. *Adv Mater*. 2013;25(15):2152-2157.

18. Zhang Z, Duan L, Xu Y, et al. Synthesis of multicore-shell FeS_2@C nanocapsules for stable potassium-ion batteries. *J Energy Chem*. 2022;73:126-132.

19. Zhang Z, Sun J, Duan L, et al. Self-templated construction of peanut-like P3-type $K_{0.45}Mn_{0.5}Co_{0.5}O_2$ for highly reversible potassium storage. *J Mater Chem A*. 2022;10(2):554-560.

20. Li Y, Yan K, Lee HW, Lu Z, Liu N, Cui Y. Growth of conformal graphene cages on micrometre-sized silicon particles as stable battery anodes. *Nat Energy*. 2016;1(2):15029.

21. Xu Q, Li JY, Sun JK, Yin YX, Wan LJ, Guo YG. Watermelon-inspired Si/C microspheres with hierarchical buffer structures for densely compacted Lithium-Ion battery anodes. *Adv Energy Mater*. 2017;7(3):1601481.

22. Chae S, Ko M, Kim K, Ahn K, Cho J. Confronting issues of the practical implementation of Si anode in high-energy lithium-ion batteries. *Joule*. 2017;1(1):47-60.

23. Xin F, Whittingham MS. Challenges and development of tin-based anode with high volumetric capacity for Li-ion batteries. *Electrochem Energy Rev*. 2020;3(4):643-655.

24. Park J, Ha S, Jung JY, et al. Understanding the effects of interfacial lithium ion concentration on lithium metal anode. *Adv Sci*. 2019;9(6):2104145.

25. Liu J, Bao Z, Cui Y, et al. Pathways for practical high-energy long-cycling lithium metal batteries. *Nat Energy*. 2019;4(3):180-186.

26. Yoon HJ, Hong SK, Lee ME, Hwang J, Jin HJ, Yun YS. Sulfur-doped carbon nanotemplates for sodium metal anodes. *ACS Appl Energy Mater*. 2018;1(5):1846-1852.

27. Xu W, Wang J, Ding F, et al. Lithium metal anodes for rechargeable batteries. *Energy Environ Sci*. 2014;7(2):513-537.

28. Jung JI, Park S, Ha S, Cho SY, Jin HJ, Yun YS. Effects of nanopores and sulfur doping on hierarchically bunched carbon fibers to protect lithium metal anode. *Carbon Energy*. 2021;3(5):784-794.

29. Gur TM. Review of electrical energy storage technologies, materials and systems: challenges and prospects for large-scale grid storage. *Energy Environ Sci*. 2018;11(10):2696-2767.

30. Albertus P, Babinec S, Litzelman S, Newman A. Status and challenges in enabling the lithium metal electrode for high-energy and low-cost rechargeable batteries. *Nat Energy*. 2018;3(1):16-21.

31. Yuan S, Kong T, Zhang Y, et al. Advanced electrolyte design for high-energy-density Li-metal batteries under practical conditions. *Angew Chem Int Ed*. 2021;60(49):25624-25638.

32. Yue X, Ma C, Bao J, et al. Failure mechanisms of lithium metal anode and their advanced characterization technologies. *Acta Phys Chim Sin*. 2021;37(2):2005012.

33. Park S, Ahn K, Lim HK, Jin HJ, Han S, Yun YS. Intagliated Cu substrate containing multifunctional lithiophilic trenches for Li metal anodes. *Chem Eng J*. 2022;428:130939.

34. Ha S, Yoon HJ, Jung JI, et al. 3D-structured organic-inorganic hybrid solid-electrolyte-interface layers for lithium metal anode. *Energy Storage Mater*. 2021;37:567-575.

35. Adair KR, Iqbal M, Wang C, et al. Towards high performance Li metal batteries: nanoscale surface modification of 3D metal

hosts for pre-stored Li metal anodes. *Nano Energy*. 2015; 54:375-382.

36. Wang T, Zhai P, Legut D, et al. S-doped graphene-regional nucleation mechanism for dendrite-free lithium metal anodes. *Adv Energy Mater*. 2019;9(24):1804000.

37. Zhang F, Liu X, Yang M, et al. Novel S-doped ordered mesoporous carbon nanospheres toward advanced lithium metal anodes. *Nano Energy*. 2020;69:104443.

38. Martin C, Genovese M, Louli AJ, Weber R, Dahn JR. Cycling lithium metal on graphite to form hybrid lithium-ion/lithium metal cells. *Joule*. 2020;4(6):1296-1310.

39. Jin S, Jiang Y, Ji H, Yu Y. Advanced 3D current collectors for lithium-based batteries. *Adv Mater*. 2018;30(48):1802014.

40. Zhang R, Wen S, Wang N, et al. N-doped graphene modified 3D porous Cu current collector toward microscale homogeneous li deposition for Li metal anodes. *Adv Energy Mater*. 2018;8(23):1800914.

41. Jiang H, Zhou Y, Guan C, et al. Ion/electron redistributed 3D flexible host for achieving highly reversible Li metal batteries. *Small*. 2022;18(29):2107641.

42. Guo J, Wang W, Li Y, et al. Room-temperature synthesis of water-dispersible sulfur-doped reduced graphene oxide without stabilizers. *RSC Adv*. 2020;10(44):26460-26466.

43. Jafari SM, Khosravi M, Mollazadeh M. Nanoporous hard carbon microspheres as anode active material of lithium ion battery. *Electrochim Acta*. 2016;203:9-20.

44. Yang J, Zhou X, Li J, Zou Y, Tang J. Study of nano-porous hard carbons as anode materials for lithium ion batteries. *Mater Chem Phys*. 2012;135(2-3):445-450.

45. Väli R, Jänes A, Thomberg T, Lust E. Synthesis and characterization of D-glucose derived nanospheric hard carbon negative electrodes for lithium- and sodium-ion batteries. *Electrochim Acta*. 2018;253(31):536-544.

46. Gaddam RR, Yang D, Narayan R, Raju K, Kumar NA, Zhao XS. Biomass derived carbon nanoparticle as anodes for high performance sodium and lithium ion batteries. *Nano Energy*. 2016;26:346-352.

47. Yue G, Cheng R, Gao X, et al. Hydrothermal synthesis of lignin-based carbon microspheres as anode material for lithium-ion batteries. *Int J Electrochem Sci*. 2020;15(2):1035-1043.

48. Yoo DJ, Liu Q, Cohen O, Kim M, Persson KA, Zhang Z. Understanding the role of SEI layer in low-temperature performance of lithium-ion batteries. *ACS Appl Mater Interfaces*. 2022;14(9):11910-11918.

49. Chen Z, Danilov DL, Raijmakers LHJ, et al. Overpotential analysis of graphite-based Li-ion batteries seen from a porous electrode modeling perspective. *J Power Sources*. 2021;509:230345.

50. Wang S, Wang Y, Song Y, et al. Synergistic regulating of dynamic trajectory and lithiophilic nucleation by Heusler alloy for dendrite-free Li deposition. *Energy Storage Mater*. 2022;50:505-513.

51. Ha S, Kim D, Lim HK, Koo CM, Kim SJ, Yun YS. Lithiophilic mxene-guided lithium metal nucleation and growth behavior. *Adv Funct Mater*. 2021;31(32):2101261.

52. Wang X, Pawar G, Li Y, et al. Glassy Li metal anode for high-performance rechargeable Li batteries. *Nat Mater*. 2020;19(12): 1339-1345.

53. Dong K, Xu Y, Tan J, et al. Unravelling the mechanism of lithium nucleation and growth and the interaction with the solid electrolyte interface. *ACS Energy Lett*. 2021;6(5): 1719-1728.

54. Yu H, Dong X, Pang Y, Wang Y, Xia Y. High power lithium-ion battery based on spinel cathode and hard carbon anode. *Electrochim Acta*. 2017;228:251-258.

55. Dsoke S, Fuchs B, Gucciardi E, Wohlfahrt-Mehrens M. The importance of the electrode mass ratio in a Li-ion capacitor based on activated carbon and $Li_4Ti_5O_{12}$. *J Power Sources*. 2015;282:385-393.

56. Ji B, Zhang F, Sheng M, Tong X, Tang Y. A novel and generalized lithium-ion-battery configuration utilizing Al foil as both anode and current collector for enhanced energy density. *Adv Mater*. 2017;29(7):1604219.

57. Appiah WA, Park J, Van Khue L, et al. Comparative study on experiments and simulation of blended cathode active materials for lithium ion batteries. *Electrochim Acta*. 2016;187:422-432.

58. Xie C, Chang J, Shang J, et al. Hybrid lithium-ion/metal electrodes enable long cycle stability and high energy density of flexible batteries. *Adv Funct Mater*. 2022;32(34):2203242.

SUPPORTING INFORMATION

Additional supporting information can be found online in the Supporting Information section at the end of this article.